Simultaneously Maximizing Surface Distortion and Pt Utilization of Pt Porous Nanosheets Enhances Oxygen Reduction Catalysis

*Yonggang Feng, Bolong Huang, Chengyong Yang, Qi Shao and Xiaoqing Huang**

Y. Feng, C. Yang, Q. Shao, Prof. X. Huang
College of Chemistry, Chemical Engineering and Materials Science, Soochow University, Jiangsu 215123, China.
E-mail: hxq006@suda.edu.cn

Prof. B. Huang
Department of Applied Biology and Chemical Technology, The Hong Kong Polytechnic University, Hung Hom, Kowloon, Hong Kong SAR.

Y. Feng and B. Huang contribute equally.

Keywords: Platinum, Porous nanosheet, Surface distortion, Electrocatalysis, Oxygen reduction reaction

Abstract

Unlike the well-established shape/composition control, surface distortion is a newly emerged yet largely unexplored nano-surface engineering for boosting electrocatalysis. Tapping into the novel electrocatalysts for taking full use of distortion effect is therefore of critical importance but remains formidable challenging. Here, we reported a unique approach to design the highly distorted Pt nanosheets (NSs) with a porous feature that derived from the ultrathin $PtTe_2$ NSs *via* electrochemical erosion. The inherent ultrathin feature and massive leaching of Te have conspired to produce highly distorted structure, achieving maximized surface distortion as well as Pt utilization. As a result, the generated Pt NSs exhibit much enhanced ORR mass and specific activity of 2.07 A mg_{Pt}^{-1} and 3.1 mA cm^{-2}, 9.8 and 10.7 times higher than those of commercial Pt/C. The highly distorted Pt NSs can also endure

30000 cycles with negligible activity decay and structure variation. DFT calculations revealed that the electrochemical corrosion induced nanopores, boundaries, and vacancies consist of Pt-sites with substantially low coordination numbers deviating from the one of pristine Pt (111) surface. These Pt-sites actively play as electron-depleting centers for highly efficient electron-transfer towards the adsorbing O-species. The close correlation between structural configuration and electronic activities has been unraveled by a newly discovered *Volcano-Plot*. This consistently maps a pathway for optimally boosting-up ORR performance *via* nano-surface engineering. Our study opens a new design for fully using the distortion effect to promote ORR performance and beyond.

1. Introduction

The global energy crisis and human-induced climate change have stimulated the development of novel energy storage and conversion devices, of which fuel cells have been recognized as one of the most promising solutions for future energy supply needs and a wide variety of applications owing to their high efficiencies and low emissions.[1-4] The sluggish kinetics of cathode oxygen reduction reaction (ORR) in fuel cells, however, has become a bottleneck that severely restricts the overall efficiency of the device and the large-scale deployment.[3-6] In general, the platinum (Pt), albeit prohibitively expensive, plays a particularly important role in the field of the discovery and optimization of novel ORR catalysts.[7-9] Numerous studies linking to the apparent effects (morphology, composition, size, etc.) upon optimizing the natural properties of Pt-based alloy and tailoring their ORR activities have gained momentum in recent years.[9-12] On the other hand, increasing researches are gradually penetrating into the contribution of surface distortion (strain, defect, rearrangement, etc.) for boosting ORR performance.[13-16] In most cases, the Pt-based alloy

inevitably undergoes the dissolution of the active phase from skin layers and cause surface distortion or defectiveness under harsh fuel cells operation conditions. Such a structure transition has been demonstrated to be beneficial rather than detrimental to the ORR kinetics.[13, 17-19] Considering that the distortion effect is almost confined on the surface of Pt-based alloy catalysts, creating a novel catalyst with the pervasive distorted structure for maximizing the distortion effect as well as Pt utilization is desirable but remains formidable challenging.

The free-standing ultrathin two-dimensional (2D) nanomaterials, intrinsically possessing much high specific surface area and surface atomic ratio, is undoubtedly the most feasible model to simultaneously achieve high structure distortion and high atom utilization.[20-23] Despite comparatively broad research have focused on the Pt-containing 2D nanomaterials, Pt usually exists as an ultrathin shell that fixed on the catalysts surface, which is not favorable for constructing efficient distortion structure.[24-26] More recently, the Pt-containing topological semimetals (e.g, $PtSe_2$, $PtTe_2$) with inherent layered structure have attracted growing research interests because of their unique physical and chemical properties.[27-29] While the PtTe monolayer can display excellent catalytic activity toward ORR as predicted by density functional theory (DFT) calculations, Te is also demonstrated to be readily dissolved by chemical or electrochemical leaching process.[30, 31] Although a few interesting catalytic properties are found in PtTe theoretically, there is lack of reports on the free-standing ultrathin PtTe nanosheets (NSs) for ORR experimentally.

In this contribution, a unique wet-chemical approach associated with CO/HCOOH is developed for the production of ultrathin and highly flexible $PtTe_2$ NSs. The Te is highly dissolvable by different corrosion procedures (electrochemical corrosion or acid corrosion), leading to the formation of porous Pt NSs, in which a significant rearrangement of surface Pt atom occurs simultaneously. The resulted E-Pt NSs (electrochemical corrosion) with the

maximized distortion structure exhibits much enhanced ORR mass and specific activity of 2.07 A mg_{Pt}^{-1} and 3.1 mA cm^{-2} that are 9.8 and 10.7 times greater than those of commercial Pt/C, 2.2 and 1.8 times higher than those of A-Pt NSs (acid corrosion), respectively. The highly distorted E-Pt NSs/C endures long-term stability test (at least 30000 cycles) with negligible activity decay and structural change. Nano-surface engineering (distortion effect) for reaching highly electronic active Pt-sites is an optimal solution for ultimately boosting-up ORR but lacking clear structural modulation pathway. To this end, our DFT calculations unraveled a *Volcano-Plot* correlating between structural featured electronic activities and corresponding formation energies. Precise electrochemical corrosion incorporates substantially lower coordinated surface Pt-sites, which actively play as electron-depleting centers for efficient electron-transfer to O-species. This conducts a universal electronic activity tuning path *via* nano-surface engineering towards preeminent ORR performance and beyond.

2. Results and Discussion

The novel ultrathin $PtTe_2$ NSs were successfully prepared through a facile wet-chemical approach, where platinum (II) acetylacetonate ($Pt(acac)_2$) and telluric (VI) acid ($Te(OH)_6$) were co-reduced under the assistance of CO/HCOOH (see Supplementary Information for details). In this synthesis, the combined use of CO/HCOOH is critical for growing ultrathin $PtTe_2$ NSs. While without using of CO produced PtTe nanoaggregates, the absence of HCOOH yielded irregular PtTe NSs with some nanoaggregates (**Figure S1**).[32, 33] The prepared $PtTe_2$ NSs exhibit uniform size and shape as well as high flexibility, associating with the presence of corrugated structure in the central region of each $PtTe_2$ NS (**Figure 1a-b**). The high flexibility of $PtTe_2$ NSs originates from its inherent ultrathin feature, where the thickness of the resulting NSs is as thin as down to 0.9 nm, as confirmed by atomic force microscope

(AFM) studies (**Figure 1c and Figure S2**). The atomic ratio of Pt and Te is calculated to be 32.1 : 67.9 by energy dispersive X-ray spectrophotometer (EDS), being consistent with that of inductively coupled plasma optical emission spectrometry (ICP-OES Pt : Te = 31.4 : 68.6) (**Figure S3a**). The powder X-ray diffraction (PXRD) pattern displays obvious peaks at the 2θ values of 25.5°, 30.9°, 43.4°, 45.0°, 48.5°, 55.6°, 59.4, 64.3°, 72.4°, 74.1°, 81.8° and 83.1°, corresponding to intermetallic $PtTe_2$ (100), (101), (102), (110), (111), (201), (103), (202), (004), (211), (212) and (300) planes (JCPDS file no. 18-0977) (**Figure S3b**). The crystalline nature of the ultrathin $PtTe_2$ NSs was further confirmed by high-resolution TEM (HRTEM) images (**Figure 1d-f and Figure S4**), where the interplanar spacing of 0.29 nm and 0.20 nm were clearly observed and assigned to the (101) and (110) plane of $PtTe_2$, respectively. The HAADF-STEM image and corresponding elemental mappings showed that Pt and Te are distributed evenly over the whole NS (**Figure 1g**). The Raman spectrum in **Figure 1h** showed the E_g and A_{1g} vibrational modes at ~ 110 and 157 cm^{-1} respectively, which are typical for 1T-$PtTe_2$ structure.[29] The stick-and-ball crystal structure model of $PtTe_2$ reveals that it has a layered structure with a hexagonal unit cell and crystallizes in $P\,\bar{3}m1$ space group, where each Pt atom is surrounded by six Te atoms (**Figure 1i**). The successful preparation of ultrathin $PtTe_2$ NSs can provide an ideal foundation for further investigating the relationship between their electrochemical performance and structure.

The $PtTe_2$ NSs were then loaded on carbon powder to prepare the $PtTe_2$ NSs/C (**Figure S5**) and their electrochemical behaviors were initially studied by cyclic voltammetry (CV) in $HClO_4$ (0.1 M) solution (see Supplementary Information for details). The activated process was monitored by tracking the changes of CV profiles, where a dramatic profile change was observed for the $PtTe_2$ NSs/C during the first 75 cycles. As shown in **Figure 2a left**, the continuous decrease for the peak current between 0.9 V and 1.2 V reveals the dissolution of Te during the successive potential cycling. At the same time, the augment in the

underpotential deposited hydrogen between 0.05 V and 0.30 V indicates the exposure of Pt-rich skin. The electrochemically active surface area (ECSA) was calculated to understand this change quantitatively. As shown in **Figure 2a right**, the ECSA of $PtTe_2$ NSs/C increases gradually along with CV cycles increase. After 75 cycles, the ECSA reaches to their maximum (70.2 $m^2 \cdot g^{-1}$) and remains stable thereafter. This dramatic profile change can be explained by the massive Te dissolution driven by the potential cycling, which could generate plentiful of surface vacancies and even porosities. Given that these surface defects can enhance the mobility and dissolution of Pt, a sequence of surface reconstruction is happened, which results in the distinct morphology/composition changes.

To this end, detailed characterizations for $PtTe_2$ NSs after activated process were further carried out. As shown in **Figure 2b-c**, an obvious porous morphological difference is observed by comparing with pristine $PtTe_2$ NSs. A slight size contraction is also detected after activated process, suggesting that the surface reconstruction has taken place. Besides, the Te composition has fallen sharply to 21 % after 50 cycles and eventually dwindles to negligible level (0.8 %) after 75 cycles (**Figure S6a**). The changes of PXRD patterns indicate the phase transformations with CV cycling. The initial catalysts possess typical diffraction peaks of $PtTe_2$ phase, while obvious peaks of Pt are detected after 25 CV cycles. The peak intensity of Pt phase increases with the CV cycling. After 75 cycles, only typical Pt diffraction peaks at 39.8°, 46.3°, 67.5° and 85.7° that corresponding to the Pt of (111), (200), (220) and (331) planes are observed (**Figure S6b**). The STEM-EDX mapping images further confirmed the enrichment of Pt in the entire NS (**Figure 2d**). Comparative analysis of the line-scan results before and after activated process reveals that the content of Te in E-Pt NSs is almost negligible (**Figure S7**). XPS characterizations were also carried out to explore the surface electronic properties and surface elemental compositions during this process. **Figure S8a** shows the Pt 4*f* spectra of $PtTe_2$ NSs involving this electrochemical erosion process. Each

peak is divided into two pairs of doublets, which represents the metallic Pt^0 (around 70.9 eV and 74.3 eV) and oxidation state Pt^{2+} (around 71.9 eV and 75.1 eV) for initial $PtTe_2$ NSs. The Pt^0 becomes weaker with increasing CV cycles, while a negative shift of 0.4 eV is detected with respect to initial $PtTe_2$ NSs that mostly resulted from the dissolution of adjacent Te atoms. As seen in the Te 3*d* XPS spectra for initial $PtTe_2$ NSs, the signals at 575.2 and 585.0 eV correspond to $3d_{5/2}$ and $3d_{3/2}$ binding energies of Te^{4+} and the signals at 572.0 and 582.4 eV correspond to $3d_{5/2}$ and $3d_{3/2}$ binding energies of Te^0 (**Figure S8b**). It is revealed that the Te^0 3*d* peaks are appreciably decreased as well as the augment of Te^{4+} 3*d* peaks during this activated process, until no obvious Te signal be detected after 75 CV cycles. The above results prove that the electrochemical Te dissolution of $PtTe_2$ NSs has resulted in E-Pt NSs with the visible morphology/composition alterations. In an attempt to ascertain the existence of distortion generated by the electrochemical Te dissolution, the catalysts were carefully studied by HRTEM. As shown, the E-Pt NSs exhibit an extended and disordered defect structure with interlayer spacing of 0.22 nm, assigned to the (111) plane of Pt. It is worth noting that many line defects and steps exist between neighboring crystalline domains and the grain boundaries contain kink sites (**Figure 2e-g and Figure S9**). These cracks on E-Pt NSs dramatically increase its surface area, which offers more coordinatively unsaturated sites for catalytic reactions while the discontinuous lattice fringes and numerous lattice mismatches are also clearly observed, showing the existence of numerous defects (**Figure 2h**).

For comparison, A-Pt NSs were also prepared *via* acid erosion (see Supplementary Information for details). The EDS and PXRD results show that Pt primarily exists in the catalyst after acid erosion (**Figure S10a-b**). TEM image of A-Pt NSs exhibits porous structure with an interplanar spacing of 0.221 nm assigned to the (111) plane of Pt (**Figure S10c-d**). It should be mentioned that weaker surface distortion/atom reconstruction and subtle size alteration occurred with acid erosion procedures with respect to the electrochemical erosion.

The line-scan analysis and STEM-EDX mapping images further confirmed the enrichment of Pt throughout the NS, where the content of Te is negligible (**Figure S10e-f**). After loaded on carbon powder, electrochemical activation was also applied to A-Pt NSs/C, where the CV variation is almost negligible from the 1st cycle to the 25th cycle (**Figure S11**). The barely changed CV profiles suggest that, for the ultrathin $PtTe_2$ NSs, acid corrosion is another effective way to wash away Te and resulted in a fairly stable surface.

Inspired by the attractive nanostructure of the generated E-Pt NSs/C and A-Pt NSs/C, we investigated their electrocatalytic activities of ORR. **Figure 3a** shows the CVs of E-Pt NSs/C, A-Pt NSs/C and commercial Pt/C. For E-Pt NSs /C, the corresponding ECSA is 70.2 $m^2 \cdot g_{Pt}^{-1}$, which is even higher than that of commercial Pt/C (66.4 $m^2 \cdot g_{Pt}^{-1}$). The ECSA of A-Pt NSs/C (57.8 $m^2 \cdot g_{Pt}^{-1}$) is a little smaller than that of E-Pt NSs /C, likely due to the weak distortion/atom reconstruction. **Figure 3b** shows the ORR polarization curves of E-Pt NSs/C, A-Pt NSs/C and commercial Pt/C. The half-wave potential for E-Pt NSs /C is 0.945 V, which is higher than those of A-Pt NSs/C (0.919 V) and commercial Pt/C (0.874 V), showing that the ORR activity follows the order of E-Pt NSs/C > A-Pt NSs/C > commercial Pt/C. The kinetic currents at 0.90 V_{RHE} from the ORR polarization curves were also normalized to the surface areas and Pt mass loadings to generate specific and mass activities, respectively (**Figure 3c**). Remarkably, E-Pt NSs/C exhibits specific activity of as high as 3.1 $mA \cdot cm^{-2}$, more than an order of magnitude higher than that for commercial Pt/C (0.29 $mA \cdot cm^{-2}$). Meanwhile, E-Pt NSs/C also exhibits highest mass activity of 2.07 $A \cdot mg_{Pt}^{-1}$, which is 2.2 and 9.8 times higher than A-Pt NSs/C (0.95 $A \cdot mg_{Pt}^{-1}$) and commercial Pt/C (0.21 $A \cdot mg_{Pt}^{-1}$), respectively. The ORR polarization curves of these different catalysts after 10000, 20000 and 30000 cycles of accelerated durability testing (ADT) are provided in **Figure 3d-e**. **and Figure S12a**. We can see that the ECSA for E-Pt NSs/C and A-Pt NSs/C were 56.5 $m^2 \cdot g_{Pt}^{-1}$ and 46.6 $m^2 \cdot g_{Pt}^{-1}$ after 30000 ADT cycles, respectively (**Figure 3f-g**), revealing that E-Pt NSs/C

(19.5%) and A-Pt NSs (19.3%) have less ECSA loss than commercial Pt/C (46.8 %) (**Figure S12b**). **Figure 3h** charts the evolution of mass activities and specific activities of E-Pt NSs/C and A-Pt NSs/C during the ADT process. There are only 12.8% mass activity and 9.8% specific activity losses for E-Pt NSs/C, while A-Pt NSs/C features a decrease in mass activity loss (9.4%) and in specific activity increase (12.3%). It is worth noting that the mass activity of A-Pt NSs/C displays a volcano shape during the ADT process, which is mostly due to the generation of higher distortion structure that resulted from the further reconstruction under electrocatalysis conditions. On the sharp contrast, commercial Pt/C shows much higher mass activity loss (48.1 %) (**Figure S12c**). To elucidate the origins of the different catalytic behavior, catalysts after the ADT process were characterized in terms of morphology, composition and elemental distribution. As shown in **Figure S13**, the morphology of E-Pt NSs/C was largely preserved after ADT process, whereas the morphology and size of A-Pt NSs/C changed a lot and became more similar to E-Pt NSs/C, indicating the robust structure of E-Pt NSs/C created by electrochemical erosion (**Figure S14**). By sharp contrast, commercial Pt/C displays obvious size change and serious aggregation after ADT process (**Figure S15**). These results collectively show that E-Pt NSs/C is highly active and durable for ORR.

We now unravel the preeminent ORR performance and mechanism from DFT calculations. Two distorted nanoporous Pt-surface models have been established with consideration of nanopores, boundaries, and Pt-vacancies (m1 and m2) (**Figure 4a and Figure S15**). The local symmetry has been remained as the one in *fcc*-Pt (111) lattice. There are various coordinated Pt-sites with distorted Pt-Pt bonds existing on the surface within those boundaries, Pt-vacancies, and nanopores regions (**Figure 4a**). The real spatial distributions of bonding and anti-bonding orbitals near the Fermi level (E_F) are demonstrated. Surface overall Pt-5*d* orbitals have been modulated by these Pt-sites showing an activated electron-rich

character, while the nanopore region exhibits localized anti-bonding orbitals for easier desorption of O-species. The surface structural configuration intrinsically guarantees an efficient electron-transfer to adsorbed O-species (**Figure 4b**).

The electronic activities of Pt-sites with various coordination numbers (CNs) have been classified with corresponding projected partial density of states (PDOSs). The 5*d* bands of Pt-sites with CN<9 present narrower band widths (4 eV in average) than those Pt-sites with CN≥9 (7 eV in average). Note, the Pt-9 represents the surface Pt with CN=9 similar with the site from Pt-surface (111-surf). The Pt-sites with CN<9 possess higher 5*d*-band center close to E_V-2.1 eV (E_V=0 for E_F), where are mainly distributing within the regions of nanopores, boundaries, or vacancies. The related dominant peaks also stay high near E_V-0.9 eV. However, as CN increases, the Pt-5*d* band center downshifts towards about E_V-3.2 eV with 2.5 eV lowered for the dominant peaks. Those Pt-sites with CN>9 behaves closely towards Pt-sites from the deep bulk regions (111-db) with their 5*d*-bands slightly modulated by the local lattice stress-effects. Therefore, the PDOSs variation trend of surface Pt-sites indicates lower coordinated Pt-sites near the nanopores, boundaries, vacancies, actively play as an electron-depleting center for electron-transfer towards the adsorbing O-species (**Figure 4c**). We compare the overall 5*d*-band given by four different systems, which are *fcc*-Pt-bulk metal, Pt-(111) surface, m1, and m2, respectively. The m1 and m2 exhibit two different weighted averaged Pt-CNs. The dominant peaks and 5*d*-band centers of Pt (111), m1, and m2 surface models are similarly staying higher levels than the *fcc*-Pt-bulk metal. This indicates the structurally modified surface Pt-sites predominantly determine the overall electronic activities, especially to the m1 model with wider range of varied surface Pt-CNs (**Figure 4d**).

Further on the different characters for electron-transfer towards O_2 and H_2O, the 2*p*-band features have been excavated. The adsorbed H_2O shows a downshifted O-2*p* band with about 2.4 eV away from the H_2O free itinerant state, denoting an obvious electron-transfer flowing

from m1 surface towards H_2O. However, the O-2*p* band of the adsorbed H_2O evidently mismatches the 5*d* band of Pt with CN<9 on the m1 surface, indicating an efficient electron-transfer character with alleviated over-binding effects for the lowered Pt-CNs. Similar trend has been also found for the O_2-adsorption. From the configurations of free itinerant, adsorbed, and desorbed, both of the 2*p*-σ and 2*p*-π states have been modified. The O_2-endon and O_2-desorption shares nearly the same electronic states denoting unflavored adsorbed structural configurations. The O-O parallel (O_2-para) adsorption experiences even larger difference for 2*p*-bands. This denotes a preeminent electron-transfer from m1-surface to well preserved O=O for optimally initializing the ORR without early O=O cleavage (**Figure 4e**). We further consider the relationship between structural characters and formation energies. Among of them, the overall weighted averaged Pt-CNs for *fcc*-Pt, m1, m2, Pt (111) are 12, 9.9, 10.2, and 10.5, respectively. Taking the *fcc*-Pt-bulk metal as reference, the m1, m2, and Pt (111) system exhibit formation energies are 0.29 eV/Pt, 0.43 eV/Pt, and 0.55 eV/Pt, respectively. This denotes the highly distorted nonporous Pt-nanosheet is obtained at the cost of stabilities. The total barrier for activating electron-transfer from surface costs the sum of surface work-function (Φ) and dominant peak position of Pt-5*d* band (*d*-pk). We found that the m1 possesses the lowest barrier. This arises because the electronic activity of m1 is the highest sitting at the *Volcano Point*, where the energetic interval is the shortest between the *d*-pk and E_F levels. Thus, the close correlation between structural features and electronic activities has now been discovered (**Figure 4f**).

For more energetic detail, we move onto the ORR pathway between m1 and Pt (111) models (**Figure 5a**). At the potential of U=0 V, m1 alleviates the Pt-O overbinding issues and improves the oxygen adsorption energy towards an optimal efficiency, compared with the energetic trend of Pt (111) system. However, considering the potential of U=1.23 V, only the m1 possesses nearly barrier free process from the step of forming [*OOH+3(H^++e^-)] towards

[*OH+H_2O*+(H^++e^-)]. Meanwhile, the potential determining step (PDS) of forming the *OOH requires the lowest energetic barrier of (0.17 eV) compared to the overall barrier found in Pt (111) system (0.58 eV). Moreover, the m1 system confronts one energetic downhill and one uphill, while the pristine Pt (111) system exhibits one downhill and two uphill trends. From the local structures (**Figure 5b**), the O-related intermediate molecules are favorably bonding with strongly distorted Pt-site on the surface near the regions of nanopores and boundaries, where has higher electronic activity for ORR catalysis. Therefore, in the system of Pt-lattice with SRDO, the strong electron-lattice coupling suppresses overbinding effect for preeminent electron-transfer between Pt-active-sites and O-species, which reaches the optimal efficiency of adsorption/desorption. By discussing the trends of electronics and energetics, we confirm that the Pt local lattice with lowered CNs substantially provides extra-active electron-transfer efficiency with barrier free or even negative trend, which accomplishes the high electronic activities and ORR performance simultaneously.

3. Conclusion

In summary, we have presented a facile wet-chemical strategy to prepare unique $PtTe_2$ NSs with ultrathin and highly flexible features. A new class of porous Pt NSs have been then constructed *via* the electrochemical erosion or acid erosion of $PtTe_2$ NSs. The massive Te dissolution from $PtTe_2$ NSs makes porous Pt NSs with successfully maximized distortions and Pt utilizations. Consequently, the generated E-Pt NSs exhibited much enhanced ORR performance in term of mass activities (2.07 $A \cdot mg_{Pt}^{-1}$) and specific activities (3.1 $mA \cdot cm^{-2}$), which is 9.8 and 10.7 times higher than those of commercial Pt/C. Significantly, the highly distorted structure is very stable with largely maintained high ORR activity even in long-time ADT process. DFT calculations reveal that, the substantially lower coordinated Pt-sites given by precisely controlled electrochemical corrosion are actively playing electron-depleting

centers for highly efficiently electron-transfer to O-species. The closely correlated electronic activities preeminently elevate the ORR performance with nearly barrier-free trended through a newly discovered *Volcano-Plot*. The subtle interplay between enhanced ORR performance and surface distortion effect essentially guides a future fuel cell optimization *via* nano-surface engineering.

4. Experimental section

Chemicals. Platinum (II) acetylacetonate ($Pt(acac)_2$, 97%) and Nafion (5%) were purchased from Sigma-Aldrich. Telluric acid (H_6TeO_6, 98%) was obtained from Aladdin. Ethanol (C_2H_6O, ≥ 99.7%), N, N-dimethylacetamide (C_4H_9NO, DMAC, ≥ 99.5%), formic acid (CH_2O_2, ≥ 98%), acetic acid ($C_2H_4O_2$, ≥ 99.9%) and acetone (C_3H_6O, ≥ 99.9%) were all purchased from Sinopharm Chemical Reagent Co. Ltd. (Shanghai, China). Commercial Pt/C (20 wt%, 2-5 nm Pt nanoparticles) was obtained from Johnson Matthey (JM) Corporation. All the chemicals were used as received without further purification. The water (18 MΩ cm^{-1}) used in all experiments was obtained by passing through an ultrapure purification system (Aqua Solutions).

Preparations of ultrathin $PtTe_2$ NSs. In a typical preparation of $PdTe_2$ NSs, $Pt(acac)_2$ (10.0 mg), $Te(OH)_6$ (5.8 mg), formic acid (0.02 mL), PVP (200 mg) and DMAC (10 mL) were added to a glass pressure vessel (volume: 48 mL). The mixture was stirred at room temperature for around 0.5 h. After being filled with CO to 1 bar, the homogeneous mixture was then heated from room temperature to 160 °C and maintained at 160 °C for 2 h in an oil bath under magnetic stirring. After cooling to room temperature, the colloidal products were collected by centrifugation, and washed twice with ethanol/acetone mixture.

Preparations of A-Pt NSs/C. The $PtTe_2$ NSs collected by centrifugation were redispersed in 4 mL ethanol by brief sonication and then mixed with 1 mL acetic acid. The mixture was heated

at 60 °C under vigorous stirring for 1 h in air to allow the transformation of $PtTe_2$ NSs into porous Pt NSs. The products were washed with ethanol/acetone mixture and collected by centrifugation. The obtained A-Pt NSs dispersed in 5 mL ethanol and Vulcan XC-72 carbon dispersed in 10 mL ethanol were mixed and sonicated for 1 h to make A-Pt NSs/C.

Preparations of E-Pt NSs/C. The $PtTe_2$ NSs dispersed in 5 mL ethanol and Vulcan XC-72 carbon dispersed in 10 mL ethanol were mixed and sonicated for 0.5 h to make $PtTe_2$ NSs/C. The prepared $PtTe_2$ NSs/C was redispersed in the mixture containing isopropanol and Nafion (5%) (v/v = 1/0.005) to form the homogeneous catalyst ink by sonicating for 60 min. The concentration of Pt was controlled to be 0.2 mg_{Pt} mL^{-1} based on ICP-OES measurement. 10 μL dispersion was casted onto the GC electrode with the Pt loading of 2 μg. The E-Pt NSs/C was prepared by cyclic voltammograms (CVs) activated process (≥ 75 cycles) at room temperature in 0.1 M $HClO_4$ solution. The products after activated process were collected and scratched off the electrode with the aid of sonication in ethanol for further characterizations.

Characterization. The samples were prepared for characterization by dropping their ethanol dispersions onto carbon-coated copper grids using pipettes. The grids were dried under ambient conditions. Low-magnification TEM was conducted on a HITACHI HT7700 transmission electron microscope at an acceleration voltage of 120 kV. High-magnification TEM and STEM were conducted on an FEI Tecnai F20 transmission electron microscope at an acceleration voltage of 200 kV. PXRD patterns were collected on X'Pert-Pro MPD diffractometer (Netherlands PANalytical) with a Cu Kα X-ray source (λ = 1.540598 Å). The concentration of catalyst was determined by ICP-OES (Varian 710-ES). All the X-ray photoelectron spectroscopy (XPS) measurements of these catalysts were collected with a Thermo Scientific, ESCALAB 250 XI system.

Electrochemical measurements. A three-electrode cell was used for the electrochemical measurements. A glassy-carbon electrode (GCE) (diameter: 5 mm, area: 0.196 cm^2) from Pine Instruments was used as the working electrode, a saturated calomel electrode (SCE) was used

as the reference electrode and a Pt wire was used as the counter electrode, respectively. The concentration of Pt was controlled to be 0.2 mg_{Pt} mL^{-1} based on ICP-OES measurement. 10 μL dispersion was casted onto the GC electrode with the Pt loading of 2 μg. The electrolyte was 0.1 M $HClO_4$ solution. The Pt loading for A-Pt NSs/C, E-Pt NSs/C and commercial Pt/C were all kept at 10.2 μg cm^{-2}. The electrochemically active surface area (ECSA) was determined by integrating the hydrogen adsorption charge on the cyclic voltammograms (CVs) at room temperature in N_2-saturated 0.1 M $HClO_4$ solution. The potential scan rate was 50 mV/s for the CV measurements. ORR measurements were conducted in 0.1 M $HClO_4$ solutions purged with saturated O_2 during the measurements. The scan rate and rotation rate for ORR measurements were 10 mV/s and 1600 rpm, respectively. In the ORR polarization curves, the current densities were normalized to the geometric area of the glassy carbon RDE (0.196 cm^2). For each catalyst, the kinetic current was normalized to loading amount and ECSA of Pt to generate mass and specific activities, respectively. The accelerated durability tests (ADTs) were performed at room temperature in 0.1 M $HClO_4$ solution by applying the cyclic potential sweeps between 0.6 V and 1.1 V versus RHE at a sweep rate of 100 mV/s. All of the electrochemical measurements were conducted at room temperature.

DFT calculations. The simple DFT+U calculations have been performed by CASTEP[34, 35]. The Hubbard-U parameter has been self-consistently determined for the onsite screened effective Coulomb potentials given by Pt-5*d*[36-38]. We choose Broyden-Fletcher-Goldfarb-Shannon (BFGS) algorithm for structural geometry optimization. The PBE functional was chosen for implementing PBE+U calculations with a plane-wave basis set cutoff energy of 750 eV. The ensemble DFT (EDFT) scheme[39] is selected for improving convergence of *d*-orbital transition metal-based system.

For the distorted nanoporous Pt models, the (111) surface-cleaved Pt structures have been built with size range of 135-191 atoms with vertical vacuum separation of 15 Å. We set the all atoms perform fully relaxation with BFGS algorithm. The m1 is the surface model with

locally twisted structure, an average diameter of 9.1 Å nanopores and randomized distributed Pt-vacancies. The m2 is similar with m1 structure, which considers the lattice collapse near the pore structure. For the Monkhorst-Pack k-point sampling, the reciprocal space integration was performed using the mesh of 2×2×1[40] with Gamma-center-off, which was self-consistently selected for total energy minimization. With these special *k*-points, the total energy is converged to less than 5.0×10^{-7} eV per atom. The Hellmann-Feynman forces on the atom were converged to less than 0.001 eV/Å.

The Pt, O, and H norm-conserving pseudopotentials are generated using the OPIUM code in the Kleinman-Bylander projector form[41], and the non-linear partial core correction[42] and a scalar relativistic averaging scheme[43] are used to treat the Pt spin-orbital coupling effect. We chose the (5*d*, 6*s*, 6*p*), (2*s*, 2*p*) and (1*s*) states as the valence states of Pt, O, and H atoms respectively. The RRKJ method is chosen for the optimization of the pseudopotentials.[44] The Hubbard U parameter has been self-consistently determined based on our previous developed method.[37, 45] By that method, the Hubbard U parameters on the Pt-$5d^9$ orbitals are uniformly determined as U_d=8.25 eV in m1 surface system.

Supporting Information

Supporting Information is available from the Wiley Online Library or from the author.

Acknowledgements

The authors thank the financial supports by the Ministry of Science and Technology of China (2016YFA0204100, 2017YFA0208200), the National Natural Science Foundation of China (21571135), Young Thousand Talented Program, the Natural Science Foundation of Jiangsu Higher Education Institutions (17KJB150032), the project of scientific and technologic infrastructure of Suzhou (SZS201708), the Priority Academic Program Development of Jiangsu Higher Education Institutions (PAPD), and start-up support from Soochow University. Y. Feng and B. Huang contribute equally to this work.

Received: ((will be filled in by the editorial staff))
Revised: ((will be filled in by the editorial staff))
Published online: ((will be filled in by the editorial staff))

[1] S. Chu, Y. Cui, N. Liu, *Nat. Mater.* **2017**, *16*, 16.

[2] Z. P. Cano, D. Banham, S. Ye, A. Hintennach, J. Lu, M. Fowler, Z. Chen, *Nat. Energy* **2018**, *3*, 279.

[3] S. Wang, S. P. Jiang, *Natl. Sci. Rev.* **2017**, *4*, 161.

[4] M. K. Debe, *Nature* **2012**, *486*, 43.

[5] C. Zhu, D. Du, A. Eychmüller, Y. Lin, *Chem. Rev.* **2015**, *115*, 8896.

[6] M. Shao, Q. Chang, J. Dodelet, R. Chenitz, *Chem. Rev.* **2016**, *116*, 3594.

[7] H. You, S. Yang, B. Ding, H. Yang, *Chem. Soc. Rev.* **2013**, *42*, 2880.

[8] Z. Fan, H. Zhang, *Chem. Soc. Rev.* **2016**, *45*, 63.

[9] X. Huang, Z. Zhao, L. Cao, Y. Chen, E. Zhu, Z. Lin, M. Li, A. Yan, A. Zettl, Y. M. Wang, X. Duan, T. Mueller, Y. Huang, *Science*, **2015**, *348*, 1230.

[10] N. S. Porter, H. Wu, Z. Quan, J. Fang, *Acc. Chem. Res.* **2013**, *46*, 1867.

[11] Y. Wang, N. Zhao, B. Fang, H. Li, X. T. Bi, H. Wang, *Chem. Rev.* **2015**, *115*, 3433.

[12] H. Huang, K. Li, Z. Chen, L. Luo, Y. Gu, D. Zhang, C. Ma, R. Si, J. Yang, Z. Peng, J. Zeng, *J. Am. Chem. Soc.* **2017**, *139*, 8152.

[13] R. Chattot, O. L. Bacq, V. Beermann, S. Kühl, J. Herranz, S. Henning, L. Kühn, T. Asset, L. Guétaz, G. Renou, J. Drnec, P. Bordet, A. Pasturel, A. Eychmüller, T. J. Schmidt, P. Strasser, L. Dubau, F, Maillard*, Nat. Mater.* **2018**, *17*, 827.

[14] M. Li, Z. Zhao, T. Cheng, A. Fortunelli, C. Chen, R. Yu, Q. Zhang, L. Gu, B. V. Merinov, Z. Lin, E. Zhu, T. Yu, Q. Jia, J. Guo, L. Zhang, W. A. Goddard, Y. Huang, X. Duan, *Science*, **2016**, *354*, 1414.

[15] P. Strasser, S. Koh, T. Anniyev, J. Greeley, K. More, C. Yu, Z. Liu, S. Kaya, D. Nordlund, H. Ogasawara, M. F. Toney, A, Nilsson, *Nat. Chem.* **2010**, *2*, 454.

[16] M. Luo, S. Guo, *Nat. Rev. Mater.* **2017**, *2*, 17059.

[17] B. Han, C. E. Carlton, A. Kongkanand, R. S. Kukreja, B. R. Theobald, L. Gan, R. O'Malley, P. Strasser, F. T. Wagner, Y. Shao-Horn, *Energy Environ. Sci.* **2015**, *8*, 258.

[18] Z. Zhang, Z. Luo, B. Chen, C. Wei, J. Zhao, J. Chen, X. Zhang, Z. Lai, Z. Fan, C. Tan, M. Zhao, Q. Lu, B. Li, Y. Zong, C. Yan, G. Wang, Z. J. Xu, H. Zhang, *Adv. Mater.* **2016**, *28*, 8712.

[19] S. Chen, Z. Niu, C. Xie, M. Gao, M. Lai, M. Li, P. Yang, *ACS nano* **2018**, *12*, 8697.

[20] D. Deng, K. S. Novoselov, Q. Fu, N. Zheng, Z. Tian, X. Bao, *Nat. Nanotechnol.* **2016**, 11, 218.

[21] M. Chhowalla, Z. Liu, H. Zhang, *Chem. Soc. Rev.* **2015**, *44*, 2584.

[22] X. Huang, S. Tang, X. Mu, Y. Dai, G. Chen, Z. Zhou, F. Ruan, Z. Yang, N. Zheng, *Nat. Nanotechnol.* **2011**, *6*, 28.

[23] Q. Lu, Y. Yu, Q. Ma, B. Chen, H. Zhang, *Adv. Mater.* **2016**, *28*, 1917.

[24] X. Tian, J. Luo, H. Nan, H. Zou, R. Chen, T. Shu, X. Li, Y. Li, H. Song, S. Liao, R. R. Adzic, *J. Am. Chem. Soc.*, **2016**, *138*, 1575.

[25] Z. Fan, Y. Zhu, X. Huang, Y. Han, Q. Wang, Q. Liu, Y. Huang, C. L. Gan, H. Zhang *Angew. Chem. Int. Ed.* **2015**, *127*, 5764.

[26] L. Bu, N. Zhang, S. Guo, X. Zhang, J. Li, J. Yao, T. Wu, G. Lu, J. Ma, D. Su, X. Huang, *Science*, **2016**, *354*, 1410.

[27] Y. Zhao, J. Qiao, P. Yu, Z. Hu, Z. Lin, S. P. Lau, Z. Liu, W. Ji, Y. Chai, *Adv. Mater.* **2016**, 28, 2399.

[28] Z. Wang, Q. Li, F. Besenbacher, M. Dong, *Adv. Mater.* **2016**, *28*, 10224.

[29] M. Yan, H. Huang, K. Zhang, E. Wang, W. Yao, K. Deng, G. Wan, H. Zhang, M. Arita, H. Yang, Z. Sun, H. Yao, Y. Wu, S. Fan, W. Duan, S. Zhou, *Nat. Commun.* **2018**, *8*, 257.

[30] Y. Wang, Y. Li, T. Heine, *J. Am. Chem. Soc.* **2018**, *140*, 12732.

[31] L. An, H. Yan, B. Li, J. Ma, H. Wei, D. Xia, *Nano Energy* **2015**, *15*, 24.

[32] Y. Dai, X. Mu, Y. Tan, K. Lin, Z. Yang, N. Zheng, G. Fu, *J. Am. Chem. Soc.* **2012**, *134*, 7073.

[33] C. Cui, L. Gan, M. Neumann, M. Heggen, B. R. Cuenya, P. Strasser, *J. Am. Chem. Soc.* **2014**, *136*, 4813.

[34] I. A. Vladimir, F. Aryasetiawan, A. I. Lichtenstein, *J. Phys. Condens. Matter* **1997**, *9*, 767.

[35] S. J. Clark, M. D. Segall, C. J. Pickard, P. J. Hasnip, M. I. J. Probert, K. Refson, M. C. Payne, *Zeitschrift Fur Kristallographie* **2005**, *220*, 567.

[36] B. Huang, R. Gillen, J. Robertson, *J. Phys. Chem. C* **2014**, *118*, 24248.

[37] B. Huang, *J. Comput. Chem.* **2016**, *37*, 825.

[38] B. Huang, *Phys. Chem. Chem. Phys.* **2016**, *18*, 13564.

[39] N. Marzari, D. Vanderbilt, M. C. Payne, *Phys. Rev. Lett.* **1997**, *79*, 1337.

[40] M. I. J. Probert, M. C. Payne, *Phys. Rev. B* **2003**, *67*, 075204.

[41] L. Kleinman, D. M. Bylander, *Phys. Rev. Lett.* **1982**, *48*, 1425.

[42] S. G. Louie, S. Froyen, M. L. Cohen, *Phys. Rev. B* **1982**, *26*, 1738.

[43] I. Grinberg, N. J. Ramer, A. M. Rappe, *Phys. Rev. B* **2000**, *62*, 2311.

[44] A. M. Rappe, K. M. Rabe, E. Kaxiras, J. D. Joannopoulos, *Phys. Rev. B* **1990**, *41*, 1227.

[45] B. Huang, *Phys. Chem. Chem. Phys.* **2017**, 19, 8008.

Figures

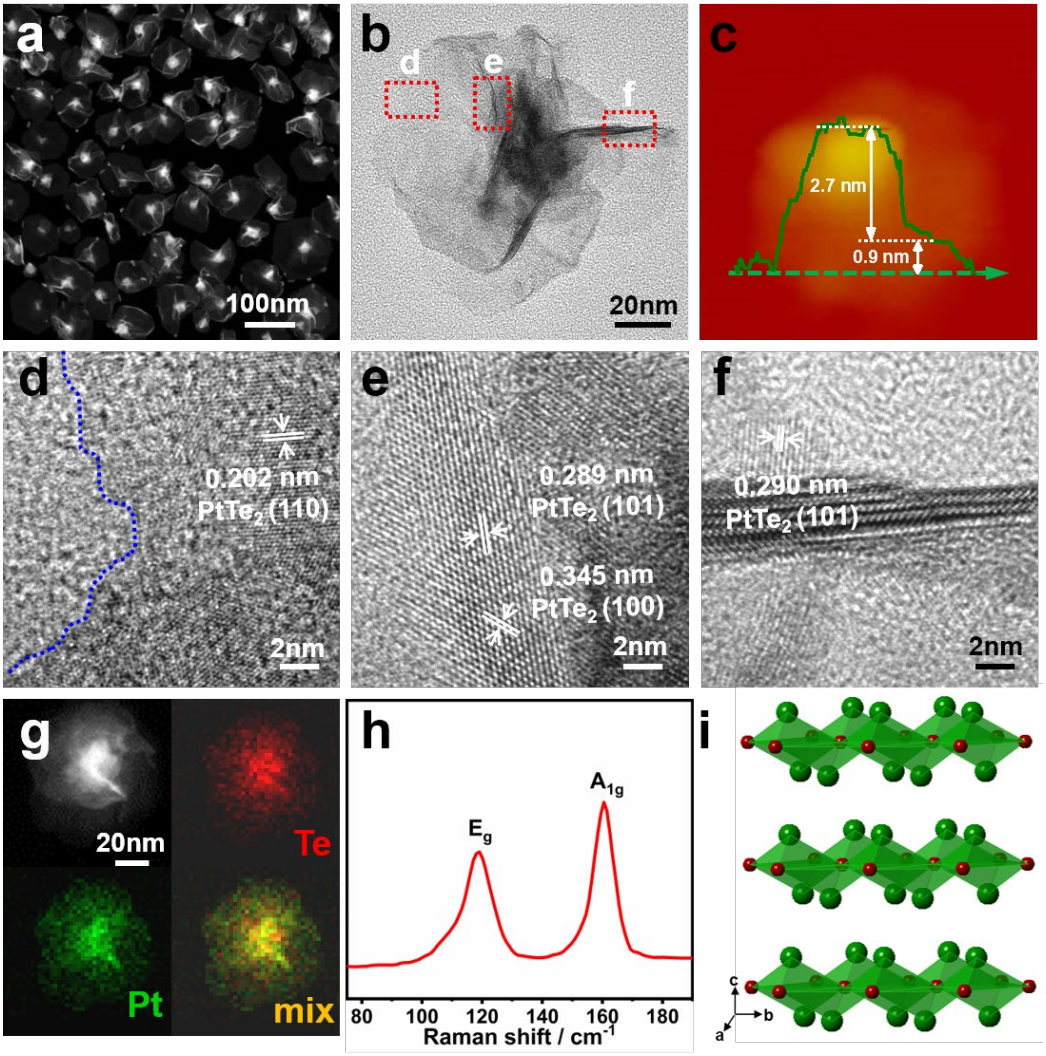

Figure 1. Morphological and Structural Characterizations of $PtTe_2$ NSs. a) HAADF-STEM image and b) high magnification TEM image of $PtTe_2$ NSs. c) Atomic force microscopy

image of $PtTe_2$ NSs with the minimum thickness of 0.9 nm. d-f) HRTEM images of $PtTe_2$ NSs from corresponding red rectangles in b). The blue dotted lines in f) represent the edge of $PtTe_2$ NSs. g) HAADF-STEM image and corresponding elemental mappings and h) Raman spectrum measured at room temperature of $PtTe_2$ NSs. i) Side views of $PtTe_2$ crystal structure. Green balls are Te atoms and red balls are Pt atoms.

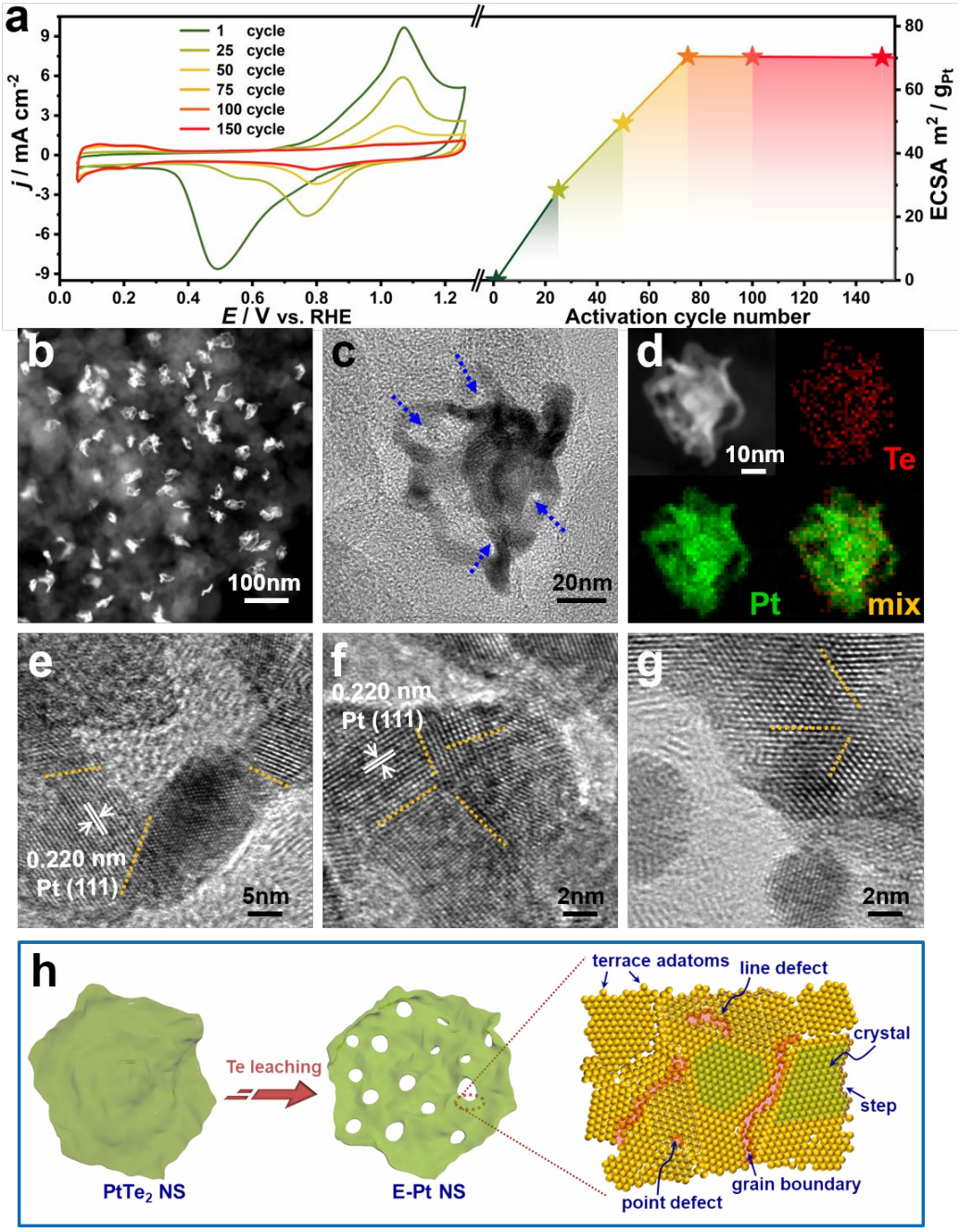

Figure 2. Morphological and Structural Characterizations of E-Pt NSs/C. a) The successive CV curves of ultrathin $PtTe_2$ NSs in 0.1 M $HClO_4$ solution at the scan rate of 50 $mV \cdot s^{-1}$. The evolution of ECSA from the corresponding activation cycles of the de-alloying process shows that 75 cycles are sufficient to reach a stable ECSA. b) HAADF-STEM image, c) high magnification TEM image, d) HAADF-STEM image and corresponding elemental mappings of E-$PtTe_2$ NSs/C. e-g) HRTEM of E-Pt NSs from corresponding red rectangles in Figure S9. The blue dotted arrows in c) represent obvious porous structure. The yellow dotted lines in e-g) represent defects. h) Schematic illustration of $PtTe_2$ NSs to E-Pt NSs transformation via electrochemical erosion and highly distorted structure of E-Pt NSs.

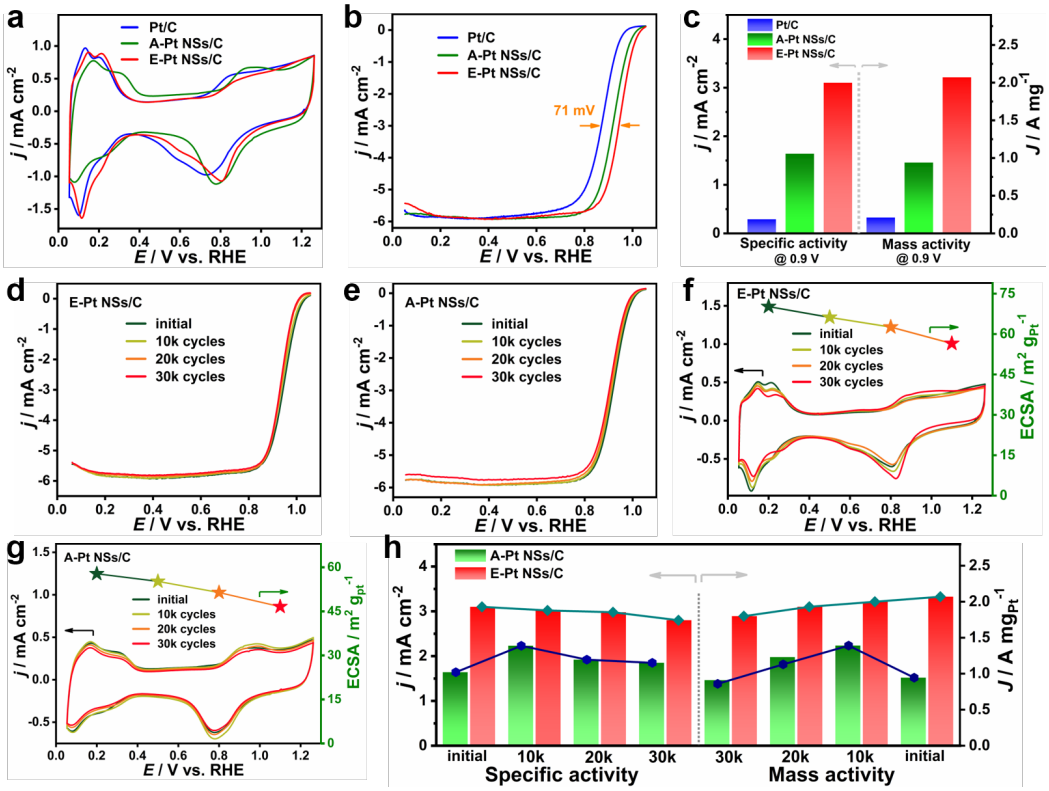

Figure 3. ORR performance of E-Pt NSs/C, A-Pt NSs/C and commercial Pt/C. a) CV curves, b) ORR polarization curves and c) the mass activity and specific activity of different catalysts.

d, e) ORR polarization curves and f, g) CV curves of d, f) E-Pt NSs/C and e, g) A-Pt NSs/C before and after different potential cycles between 0.6-1.1 V_{RHE}. The scatter lines in f, g) represent the ECSA evolutions of these catalysts after corresponding potential cycles. h) The evolution of mass activities and specific activities of E-Pt NSs/C and A-Pt NSs/C after different potential cycles.

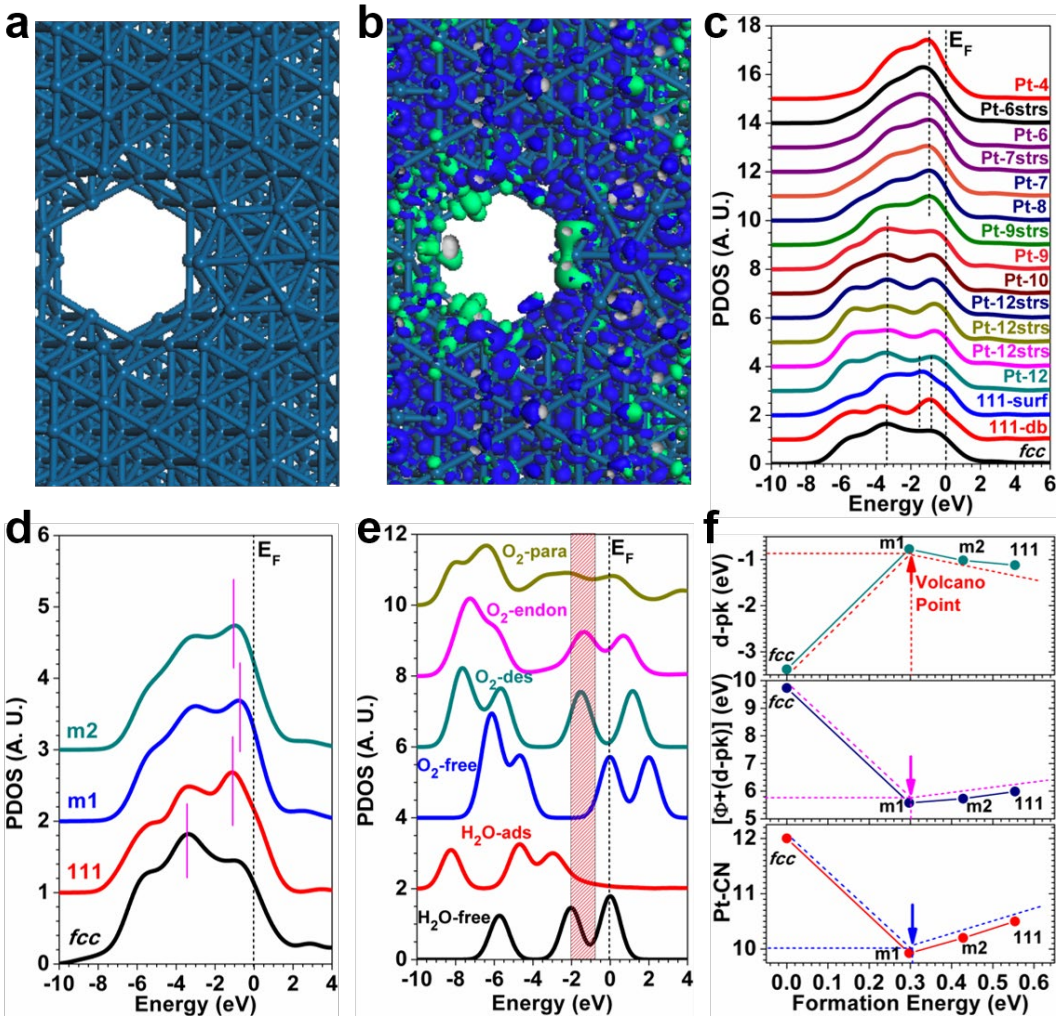

Figure 4. Electronic structures and activities for ORR electron-transfer process. a) The top-view of the Pt-m1 surface model. b) The real spatial contour plots for bonding and anti-bonding orbitals near E_F for the m1 surface model. c) PDOSs evolutions of site-dependent 5*d*-bands of Pt-sites with different coordination numbers (CNs) as well as the stress effect (strs). Dash lines denote the dominant peak positions. d) Different overall contributions to the

PDOSs by Pt-5*d* bands among *fcc*-Pt-bulk metal, Pt-(111), m1, and m2 systems. e) PDOSs of O-2*p* bands for H_2O and O_2 on the cases before adsorption (free), adsorption (ads), and desorption (des). f) Energetic trends for the overall Pt-5*d* dominant peak positions (*d*-pk), total activation barriers [Φ+(*d*-pk)], and weighted averaged Pt coordination number (Pt-CN), with related to the formation energies of the *fcc*-Pt-bulk metal, Pt-(111), m1, and m2 systems, respectively.

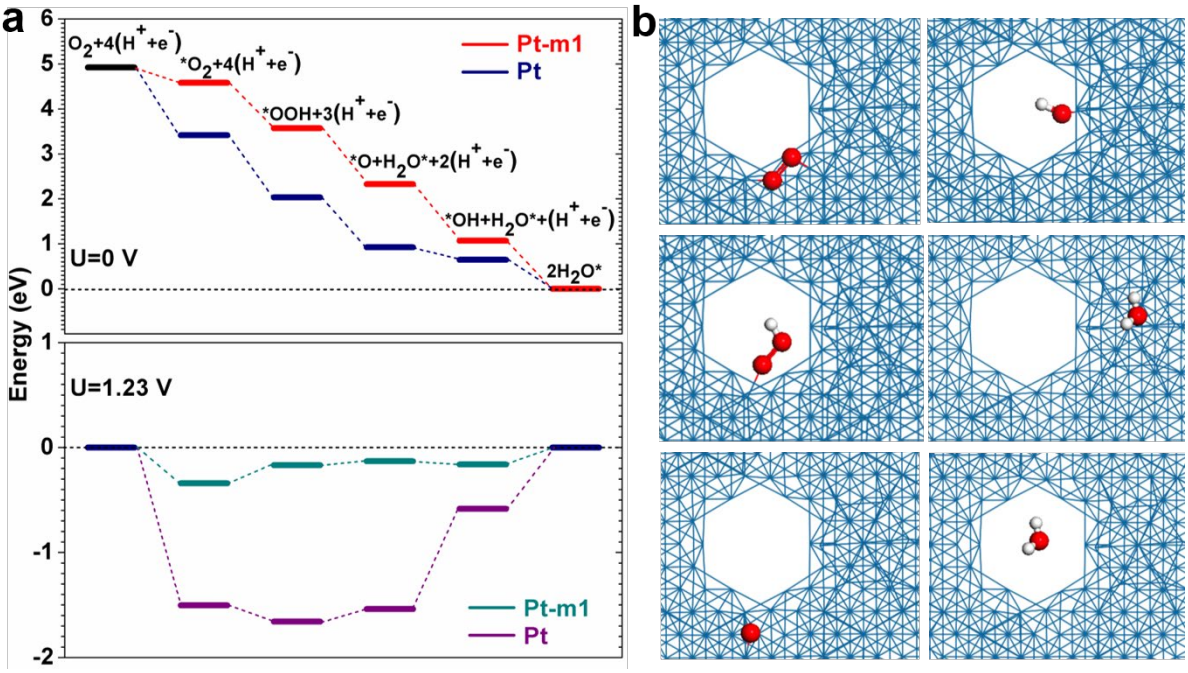

Figure 5. ORR energy profile for local activity pathway plot. a) The free energetic pathways for acidic four-electron ORR based on the m1 and Pt (111) surface models, respectively, in both zero electrode potential (U=0 V) and equilibrium potential (U=1.23 V). b) Local structural configurations of initial reactant, intermediates or final product on the m1 surface models.

The table of contents entry

Ultrathin Pt porous nanosheets have been created for the first time and applied for ORR electrocatalysis. The nano-surface engineering with the simultaneous maximization of surface distortion and Pt utilization achieved preeminent ORR performance.

Keyword: Platinum, Porous nanosheet, Surface distortion, Electrocatalysis, Oxygen reduction reaction

Yonggang Feng, Bolong Huang, Chengyong Yang,Qi Shao and Xiaoqing Huang*

Simultaneously Maximizing Surface Distortion and Pt Utilization of Pt Porous Nanosheets Enhances Oxygen Reduction Catalysis

TOC Figure